IOP Publishing

Journal of Physics B: Atomic, Molecular and Optical Physics

J. Phys. B: At. Mol. Opt. Phys. **58** (2025) 015001 (9pp)

https://doi.org/10.1088/1361-6455/ad978f

Radiative decay rates for magnetic dipole (M1) and electric quadrupole (E2) transitions between low-lying levels within the $4f^3$ ground configuration of Pr III

L Maison[1], **P Palmeri**[1] **and P Quinet**[1,2,*]

[1] Physique Atomique et Astrophysique, Université de Mons—UMONS, B-7000 Mons, Belgium
[2] IPNAS, Université de Liège, B-4000 Liège, Belgium

E-mail: pascal.quinet@umons.ac.be

Received 27 August 2024, revised 5 November 2024
Accepted for publication 26 November 2024
Published 5 December 2024

Abstract

A new set of theoretical radiative decay rates characterizing forbidden transitions in doubly charged praseodymium (Pr III) is reported in the present paper. More precisely, transition probabilities were computed for all magnetic dipole (M1) and electric quadrupole (E2) lines involving the lowest energy levels of the $4f^3$ ground configuration located below 20 000 cm^{-1} since the levels above this limit are preferentially depopulated by allowed electric dipole (E1) transitions. The calculations were carried out using different computational strategies based firstly on the pseudo-relativistic Hartree–Fock method and secondly on the fully relativistic multiconfiguration Dirac-Hartree–Fock method. The comparison between the results obtained by these independent approaches makes it possible to estimate their reliability. Comparisons with the few previously published data were also made. In addition, some astrophysical implications were deduced from the new atomic parameters computed in the present work, such as the possible presence of [Pr III] lines in the infrared spectra recorded by the *James Webb Space Telescope* in the context of the investigation of kilonovae in their nebular phase, i.e. several days after neutron star mergers.

Keywords: atomic data, atomic processes, forbidden lines, kilonovae

1. Introduction

The last few years have seen a significant revival of interest in the study of the atomic processes characterizing heavy (trans-iron) elements of the periodic table. One of the main motivations lies in the fact that these elements are expected to be produced in large quantities during the merger of neutron stars, first observed in August 2017 by the detection of gravitational waves by the *LIGO* and *VIRGO* interferometers (Abbott *et al* 2017). These heavy elements are formed by the nucleosynthesis rapid (r-) process and their presence was observed in the spectrum emitted just after the neutron star coalescence, called kilonova, from spectral analyses at different wavelength regions (Kasen *et al* 2017, Pian *et al* 2017, Smartt *et al* 2017, Siegel 2022, Pian 2023).

Over time, the kilonova spectrum changes appearance due to changes in the physical conditions of the environment. In the first days, the kilonova spectrum is characterized by millions of absorption lines due to the large amount of possible

* Author to whom any correspondence should be addressed.

electric dipole (E1) transitions involving a multitude of energy levels belonging to the heavy elements present in the ejecta, giving rise to a significant opacity in the observed spectrum (Kasen *et al* 2017). After several days, with the rapid decrease in temperature and density, the ejecta tends towards a nebular phase and the kilonova spectrum is dominated by emission lines, providing an excellent opportunity for element identification by spectral analysis. Recently, the infrared spectrum of the kilonova in its nebular phase, recorded using the *Spitzer Space Telescope* was assumed by Kasliwal *et al* (2022) to contain forbidden lines of magnetic (M1) and electric quadrupole (E2) types but they emphasized the lack of atomic data for forbidden transitions in heavy elements to interpret the observed emission features in detail. In this context, new and reliable radiative parameters relating to forbidden lines are required for many different atomic species. This was also underlined by Gillanders *et al* (2021) who showed that the identification of chemical elements in kilonovae could be facilitated by considering M1 and E2 transitions in the radiative transfer modeling.

Moreover, spectroscopic observations of a rapidly-reddening thermal transient, following the GRB 23 0307A gamma-ray burst, produced by the merger of compact objects, were reported by Gillanders *et al* (2023). These observations, carried out 29 d after merger ($T_0 + 29$ d) using the *James Webb Space Telescope* (*JWST*), revealed two remarkable emission features in the spectrum at $\lambda \sim 2.1$ μm and $\lambda \sim 4.4$ μm whose components were assumed by Gillanders *et al* (2023) to be mainly forbidden lines belonging to different heavy ions. These authors recognized that too little reliable radiative data were available in the literature for these forbidden transitions in order to interpret the observed spectrum accurately. This is particularly the case for lanthanide ions which are among the most abundant species present in the ejecta resulting from compact object mergers.

The present work aims to partially fill the lack of atomic data for forbidden lines in lanthanide ions by focusing on Pr^{2+} ion, following our recent study devoted to the M1 and E2 transitions in Nd III (Maison *et al* 2024). Examining the NIST database (Kramida *et al* 2024), we notice that the $4f^3$ ground configuration of Pr III extends up to 53 000 cm^{-1}. On the other hand, the lowest level of the even parity, namely $4f^2(^3H)5d$ $^2H_{9/2}$ is located at 12 846.66 cm^{-1}. It is necessary to go up to approximately 20 000 cm^{-1} so that all the values of J have at least one experimentally known level in this even parity, according to the NIST compilation. This means that, above 20 000 cm^{-1}, it is the allowed electric dipole transitions which largely predominate. It is not useful to focus on the forbidden transitions (M1 and E2) beyond this limit of 20 000 cm^{-1} since the latter are completely negligible compared to the E1 transitions. This is the reason why only the M1 and E2 transitions involving energy levels of Pr III below 20 000 cm^{-1} were considered in our calculations and why we in this paper only give transition probabilities for lines above 5000 Å. The computations were carried out using two different computational approaches based on the pseudo-relativistic Hartree–Fock (HFR) and the fully relativistic multiconfiguration Dirac-Hartree–Fock (MCDHF) methods.

2. Atomic structure calculations

2.1. Pseudo-relativistic HFR method

The first approach used to calculate the radiative parameters for M1 and E2 transitions in Pr III was the one implemented in the Cowan's suite of computer programs (Cowan 1981), namely the HFR method. The latter, based on the resolution of the Schrödinger equation, includes relativistic one-body effects such as mass correction, the Darwin term and the spin–orbit interaction, in a perturbative way. In our calculations, configuration interaction was considered by explicitly introducing the following configurations in the physical model: $4f^3$ + $4f^26p$ + $4f5d^2$ + 4f5d6s + $4f^25f$ + $4f^27p$ + $4f^26f$ + $4f6s^2$ + 4f5d7s + 4f5d6d + 4f5d7d + $4f6d^2$ + 4f6s7s + $4f7s^2$ + $4f6p^2$ + 4f6p7p + 5d6s6p + 5d26p + 6 s^26p + $6p^3$.

Using the well-established least-squares fitting procedure developed by Cowan (1981), some radial parameters such as average energies (E_{av}), Slater electrostatic interaction integrals (F^k, G^k, R^k), effective interaction parameters (α, β, γ) and spin–orbit paramaters (ζ_{nl}) were adjusted to reproduce as faithfully as possible the available experimental energy levels following exactly the same procedure as described in our previous work (Palmeri *et al* 2000, Biémont *et al* 2001). As all the details of the fit can be found in these two papers, we will simply recall here that the radial parameters characterizing the $4f^3$, $4f^26p$, $4f5d^2$, 4f5d6s, $4f^25f$, $4f^27p$ and $4f^26f$ odd-parity configurations were adjusted using all 342 experimentally known levels in these configurations taken from Martin *et al* (1978) and Palmeri *et al* (2000). This led to an average deviation of 81 cm^{-1} between calculated and experimental values for the odd-parity levels. But it is interesting to note that, when considering only the lowest energy levels in $4f^3$ ($E < 20\,000$ cm^{-1}) between which the forbidden transitions were calculated in the present work, the overall agreement between computed and experimental values was found to be excellent, with an average deviation of 1 cm^{-1}.

2.2. Fully relativistic MCDHF method

The second theoretical method used in this work to compute [Pr III] transition probabilities was the MCDHF method developed by Grant (2007), using the GRASP2018 package (Froese Fischer *et al* 2019). The computations started with the building of a single reference (SR) composed of the $4f^3$ ground configuration where all the orbitals from 1 s to 4f were optimized. From this SR, different valence–valence (VV) models were developed to optimize the orbitals in a layer-by-layer approach. This optimization was done by gradually increasing the number of configuration state functions (*CSFs*) in each computation. The *CSFs* accounting for the VV correlations were obtained by considering single and double (SD) electron substitutions from the 4f subshell up to an orbital set {n_1s, n_2p, n_3d, ...} where n_i are the maximum values of the principal quantum number associated with an azimuthal orbital quantum number (l). In total, four layers of correlations were needed until a convergence of the computed energy levels was

Table 1. Comparison between the MCDHF energies (E in cm^{-1}) obtained in the SR, VV1, VV2, VV3, VV4 and VV4+CV models and the experimental values (Kramida *et al* 2024) for the lowest levels (E_{EXP} below 20 000 cm^{-1}) within the $4f^3$ ground configuration of Pr III. The term designations, in *LS*-coupling are taken from the NIST database (Kramida *et al* 2024).

Term	J	SR	VV1	VV2	VV3	VV4	VV4+CV	EXP
^{4}I	9/2	0	0	0	0	0	0	0.00
^{4}I	11/2	1254	1259	1262	1263	1263	1275	1398.34
^{4}I	13/2	2635	2633	2637	2638	2639	2664	2893.14
^{4}I	15/2	4116	4095	4097	4098	4098	4130	4453.76
^{4}F	3/2	13 335	11 765	11 692	11 677	11 674	10 410	9370.66
^{2}H2	9/2	13 075	11 537	11 256	11 222	11 196	10 859	10 032.92
^{4}F	5/2	13 974	12 428	12 364	12 350	12 348	11 066	10 138.18
^{4}F	7/2	14 622	13 067	12 991	12 976	12 972	11 731	10 859.06
^{4}S	3/2	14 619	13 019	12 873	12 861	12 858	11 912	10 950.24
^{4}F	9/2	15 327	13 780	13 682	13 665	13 659	12 530	11 761.69
^{2}H2	11/2	15 194	13 706	13 424	13 390	13 363	13 102	12 494.63
*	7/2	17 999	16 003	15 722	15 686	15 663	14 924	13 887.60
^{4}G	5/2	20 271	18 017	17 856	17 825	17 818	15 820	14 187.35
^{4}G	7/2	21 172	18 956	18 795	18 764	18 758	16 851	15 443.48
^{4}G	9/2	22 146	19 960	19 799	19 769	19 763	17 922	15 705.13
^{2}K	13/2	19 748	18 861	18 447	18 412	18 396	17 523	16 089.14
*	9/2	19 752	17 826	17 558	17 524	17 503	16 699	16 763.98
^{2}D1	3/2	23 239	20 493	20 021	19 974	19 941	18 797	17 095.63
^{4}G	11/2	23 103	20 925	20 772	20 744	20 739	18 768	17 409.58
^{2}K	15/2	21 210	20 334	19 933	19 898	19 883	18 985	17 642.06
^{2}P	1/2	24 752	21 983	21 487	21 439	21 404	20 361	18 693.65
^{2}D1	5/2	24 905	22 134	21 699	21 652	21 621	20 512	19 046.09

observed, with the {5*s*, 5*p*, 5*d*, 5*f*, 5*g*}, {6*s*, 6*p*, 6*d*, 6*f*, 6*g*}, {7*s*, 7*p*, 7*d*, 7*f*, 6*g*}, and {8*s*, 8*p*, 8*d*, 8*f*, 6*g*} orbital sets, giving rise to the VV1, VV2, VV3, and VV4 models, respectively. From the VV4 model, core-valence (CV) correlations were added in a relativistic configuration interaction (RCI) computation to form the VV4+CV model. This was done by taking single and restricted double (SrD) substitutions from the 4*f*, 5*s* and 5*p* orbitals to the last orbital set 8*s*, 8*p*, 8*d*, 8*f*, 6*g*, where the restricted term means that only a maximum of one hole was considered in the 5*s* and 5*p* subshells while double excitations were allowed from 4*f*. This VV4+CV model led to a total of 372 492 *CSFs* when limiting the calculations to total angular momentum numbers between $J = 1/2$ and $J = 15/2$. The convergence of the calculations in terms of energy structure was verified according to the complexity of the model considered. Indeed, it was noted that, for the $4f^3$ levels of interest ($E < 20\,000$ cm^{-1}), the mean fractional deviation of the MCDHF energy to experimental energy was 0.260, 0.146, 0.132, 0.131, 0.130, and 0.060 for SR, VV1, VV2, VV3, VV4, and VV4+CV models, respectively. The convergence of the energy levels calculated in the different MCDHF models towards the experimental values is shown in table 1. Other CV models were explored, considering the opening of the 4*d* orbital in one model and opening only the 5*s* subshell in another. Core–core correlations were also investigated by removing the restriction on double substitutions for the 5*s* and 5*p* orbitals. However, none of these three RCI models succeeded in providing a better agreement with the experimental energies. Therefore the VV4+CV model, renamed MCDHF-A, was considered in our calculations. The energies obtained with this model are compared with the experimental values taken from Martin *et al* (1978) and compiled in the NIST database (Kramida *et al* 2024) as well as with the HFR results obtained in the present work in table 2. Finally, to calculate the M1 and E2 transition probabilities, the theoretical MCDHF-A wavelengths were replaced by those deduced from experimental energy levels.

Very recently, a fine-tuning procedure of atomic energies was introduced into MCDHF calculations to ensure not only a better agreement between *ab initio* and experimental levels but also a better representation of admixtures in atomic states. The procedure in the relativistic *jj*-coupling was implemented in the GRASP2018 package through the new programs *jj2lsj_2022* and *rfinetune* by Li *et al* (2023) who developed a method where the Hamiltonian in *jj*-coupling is transformed to a Hamiltonian in *LSJ*-coupling for which fine-tuning applies and where this fine-tuned *LSJ* matrix is then transformed back to a Hamiltonian in *jj*-coupling. This fine-tuning approach was also used in our work, giving rise to the MCDHF-B calculation which actually corresponds to the VV4+CV model described above in which all the experimentally known energy levels belonging to the $4f^3$ ground configuration of Pr III (Kramida *et al* 2024) were considered in the fitting process. As expected, and as detailed in table 2, this further improved the agreement between computed and experimental level energies with a mean relative deviation in the order of one percent for the lowest levels ($E < 20\,000$ cm^{-1}). To summarize, the average uncertainties on the energies calculated using the HFR, MCDHF-A and MCDHF-B methods were estimated to be 0.5%, 8.3% and 1.4%, respectively.

Table 2. Comparison between the experimental (Kramida *et al* 2024) and the calculated values obtained in the present work using the HFR and the MCDHF methods for the lowest energy levels (below 20 000 cm^{-1}) within the 4f^3 ground configuration of Pr III. The term designations, in *LS*-coupling are taken from the NIST database (Kramida *et al* 2024).

Term	J	E_{Exp}	E_{HFR}	$E_{MCDHF-A}$	$E_{MCDHF-B}$
^{4}I	9/2	0.00	0	0	0
^{4}I	11/2	1398.34	1392	1275	1396
^{4}I	13/2	2893.14	2889	2664	2891
^{4}I	15/2	4453.76	4459	4130	4441
^{4}F	3/2	9370.66	9450	10 410	9389
^{2}H2	9/2	10 032.92	10 179	10 859	9616
^{4}F	5/2	10 138.18	10 227	11 066	10 211
^{4}F	7/2	10 859.06	10 971	11 731	10 826
^{4}S	3/2	10 950.24	10 893	11 912	10 990
^{4}F	9/2	11 761.69	11 878	12 530	11 691
^{2}H2	11/2	12 494.63	12 606	13 102	12 166
*	7/2	13 887.60	14 002	14 924	13 192
^{4}G	5/2	14 187.35	14 143	15 820	14 320
^{4}G	7/2	15 443.48	15 453	16 851	15 423
^{4}G	9/2	15 705.13	15 768	17 922	15 903
^{2}K	13/2	16 089.14	16 128	17 523	16 158
*	9/2	16 763.98	16 845	16 699	14 809
^{2}D1	3/2	17 095.63	17 055	18 797	17 297
^{4}G	11/2	17 409.58	17 434	18 768	17 458
^{2}K	15/2	17 642.06	17 663	18 985	17 691
^{2}P	1/2	18 693.65	18 521	20 361	18 748
^{2}D1	5/2	19 046.09	19 076	20 512	19 089

3. Radiative decay rates

The weighted transition probabilities of Pr III forbidden lines computed in the present work using the HFR, MCDHF-A and MCDHF-B approaches are listed in table 3. In total, 133 lines are given in this table, which corresponds to all possible M1 and E2 transitions involving the experimentally known energy levels below 20 000 cm^{-1} and within the 4f^3 ground configuration.

By comparing the gA-values with each other, we see a fairly good general agreement, the average relative deviations between the HFR and MCDHF data, namely

$$\frac{\Delta gA}{\overline{gA}} = \frac{gA\,(\mathrm{HFR}) - gA\,(\mathrm{MCDHF})}{(gA\,(\mathrm{HFR}) + gA\,(\mathrm{MCDHF}))\,/2} \quad (1)$$

being found to be equal to 0.48 ± 0.80 and 0.21 ± 1.09 if we consider the MCDHF-A and MCDHF-B calculations, respectively. Of course, it should be noted that significant discrepancies (sometimes up to an order of magnitude) can be observed for specific transitions but these cases are mostly characterized by very low transition probabilities. However, for the majority of the strongest transitions ($gA \geqslant 10^{-1}$ s^{-1}), the agreement between the HFR and both the MCDHF-A and MCDHF-B results is generally within a factor of 2. Such comparisons are shown in figure 1, in which the HFR gA-values are plotted against the MCDHF-A and MCDHF-B data.

Let us add that, in the MCDHF calculations, the E2 transition probabilities were obtained in the Babushkin and Coulomb gauges and it is useful to point out that the agreement between these two gauges was often quite poor, with differences of up to one order of magnitude for the weakest E2 transitions. However, these E2 contributions were found to be generally much smaller than the M1 contributions and therefore play a less important role in the decay rate parameters when both types of radiation are involved.

It is also interesting to note that our transition probabilities calculated with the HFR method present a very good agreement with those published by Li *et al* (2016), with an average relative deviation of 0.09 ± 0.34 for the set of 38 M1 and E2 lines common to both studies. This is illustrated in figure 2, where the HFR results obtained in the present work are compared to the gA-values computed by Li *et al* (2016) who focused on Pr III forbidden transitions in the wavelength range from 3000 to 17 000 Å.

To our knowledge, the only radiative data available to date for forbidden transitions in Pr III were precisely those published by Li *et al* (2016). Our work therefore significantly extends this previous study by providing, for the first time, a complet and consistent set of transition probabilities for all possible M1 and E2 spectral lines involving the lowest levels (<20 000 cm^{-1}) belonging to the ground configuration of Pr III.

4. Astrophysical implications

The *JWST* is the largest and most powerful telescope ever sent into space. It is equipped with different scientific instruments observing the sky from long-wavelength visible light (red) through mid-infrared (0.6–28.3 μm). Among these instruments, the *Near-Infrared Spectrograph* (*NIRS*) is designed to be capable of carrying out low-resolution (R = 30–330) prism spectroscopy over the wavelength range 0.6–5.3 μm and higher resolution (R = 500–1340 or R = 1320–3600) grating spectroscopy over 0.7–5.2 μm (Jakobsen *et al* 2022).

In table 3, we see that, in the wavelength range covered by *NIRS*, a fairly large number of lines have a relatively high transition probability. More precisely, among the 133 lines listed in the table, 42 have a HFR gA-value greater than 10^{-1} s^{-1}. For these lines, collected in table 4, it should be noted that an overall good agreement (within a few tens of percent) is found when comparing the HFR gA-values with those obtained using the MCDHF-A and MCDHF-B approaches, except for a couple of lines for which larger discrepancies are observed.

Some [Pr III] transitions listed in table 4 could also be of particular astrophysical interest as they could contribute to the features observed at ∼2.1 μm and ∼4.4 μm in the T_0+29 d *JWST* emission spectrum of GRB 23 0307A by Gillanders *et al* (2023). They notably assumed that these features were composed of several forbidden lines belonging to heavy elements such as lanthanides. If we take into account the extensions of these two features, namely between 1.94 and 2.35 μm for the first one and between 4.18 and 4.55 μm for the second one, we can see from table 4 that only 5

Table 3. Transition probabilities (gA) for [Pr III] lines calculated in the present work using HFR and MCDHF methods.

	Lower level[b]		Upper level[b]		gA (s^{-1}) ($A(B) = A \times 10^B$)				Type
λ_{vac} (Å)[a]	E (cm^{-1})	J	E (cm^{-1})	J	Previous[c]	HFR[d]	MCDHF-A[d]	MCDHF-B[d]	> 1%
5250.421	0.00	9/2	19 046.09	5/2		3.36(−7)	3.01(−6)	1.31(−4)	E2
5743.964	0.00	9/2	17 409.58	11/2	3.83(−3)	3.67(−3)	1.26(−3)	4.46(−2)	M1
5965.171	0.00	9/2	16 763.98	9/2	8.03(−2)	8.87(−2)	2.17(−1)	1.57(−1)	M1+E2
6156.225	1398.34	11/2	17 642.06	15/2		1.43(−3)	8.31(−4)	8.60(−4)	E2
6215.373	0.00	9/2	16 089.14	13/2		4.28(−3)	2.40(−3)	2.72(−3)	E2
6245.612	1398.34	11/2	17 409.58	11/2	1.63(−2)	2.10(−2)	6.46(−3)	4.73(−3)	M1+E2
6367.346	0.00	9/2	15 705.13	9/2	2.06(−1)	1.76(−1)	1.41(−2)	2.00(−1)	M1+E2
6475.224	0.00	9/2	15 443.48	7/2	1.78(−3)	3.64(−2)	3.47(−2)	1.12(−1)	M1+E2
6508.027	1398.34	11/2	16 763.98	9/2	5.33(−2)	9.91(−2)	6.18(−1)	6.18(−1)	M1+E2
6780.157	2893.14	13/2	17 642.06	15/2	7.47(+0)	7.23(+0)	4.96(+0)	6.28(+0)	M1
6806.981	1398.34	11/2	16 089.14	13/2	7.06(+0)	6.67(+0)	4.55(+0)	5.82(+0)	M1
6888.741	2893.14	13/2	17 409.58	11/2	4.19(−1)	4.38(−1)	1.93(−1)	2.14(−1)	M1+E2
6989.688	1398.34	11/2	15 705.13	9/2	7.99(−1)	7.28(−1)	2.34(−2)	7.75(−2)	M1+E2
7048.533	0.00	9/2	14 187.35	5/2	1.75(−1)	2.70(−1)	1.65(−1)	1.73(−1)	E2
7119.901	1398.34	11/2	15 443.48	7/2	1.50(−1)	2.22(−1)	1.64(−1)	1.72(−1)	E2
7200.668	0.00	9/2	13 887.60	7/2	1.82(−1)	1.72(−1)	9.02(−2)	1.18(−1)	M1+E2
7209.369	2893.14	13/2	16 763.98	9/2	1.03(−1)	1.39(−1)	5.10(−2)	3.36(−2)	E2
7578.054	2893.14	13/2	13 196.00	13/2	4.06(+0)	3.86(+0)	2.65(+0)	3.39(+0)	M1
7582.478	4453.76	15/2	17 642.06	15/2	1.17(+1)	1.12(+1)	7.76(+0)	9.87(+0)	M1
7718.539	4453.76	15/2	17 409.58	11/2	1.88(−1)	3.02(−1)	1.87(−1)	1.97(−1)	E2
7805.189	2893.14	13/2	15 705.13	9/2		1.48(−1)	1.10(−1)	1.02(−1)	E2
8003.438	0.00	9/2	12 494.63	11/2	4.36(−2)	4.83(−2)	4.65(−2)	2.15(−2)	M1
8006.880	1398.34	11/2	13 887.60	7/2		5.14(−2)	1.28(−2)	6.52(−3)	E2
8502.180	0.00	9/2	11 761.69	9/2	1.13(+0)	9.99(−1)	6.25(−1)	9.76(−1)	M1
8594.477	4453.76	15/2	16 089.14	13/2	2.69(−2)	3.01(−2)	2.22(−2)	2.61(−2)	M1
9012.021	1398.34	11/2	12 494.63	11/2	2.47(+0)	2.36(+0)	1.80(+0)	1.97(+0)	M1
9208.900	0.00	9/2	10 859.06	7/2	1.50(−2)	1.22(−2)	6.01(−3)	4.22(−3)	M1
9649.389	1398.34	11/2	11 761.69	9/2	1.11(+0)	9.76(−1)	5.99(−1)	8.32(−1)	M1
9863.703	0.00	9/2	10 138.18	5/2		4.04(−5)	1.25(−6)	6.13(−5)	E2
9967.188	0.00	9/2	10 032.92	9/2	5.93(+0)	5.71(+0)	4.32(+0)	4.62(+0)	M1
10 335.458	9370.66	3/2	19 046.09	5/2	2.36(−1)	2.41(−1)	2.01(−1)	2.39(−1)	M1
10 415.050	2893.14	13/2	12 494.63	11/2	5.75(+0)	5.51(+0)	4.27(+0)	4.59(+0)	M1
10 570.020	1398.34	11/2	10 859.06	7/2		1.96(−5)	3.09(−5)	9.33(−3)	E2
10 726.173	9370.66	3/2	18 693.65	1/2	9.40(−2)	8.92(−2)	4.42(−2)	6.05(−2)	M1
11 094.876	10 032.92	9/2	19 046.09	5/2		2.57(−4)	1.69(−4)	3.81(−4)	E2
11 225.978	10 138.18	5/2	19 046.09	5/2	5.57(−1)	5.48(−1)	4.09(−1)	4.52(−1)	M1
11 275.800	2893.14	13/2	11 761.69	9/2		4.05(−5)	4.34(−8)	1.24(−4)	E2
11 581.339	1398.34	11/2	10 032.92	9/2	3.80(+0)	3.71(+0)	2.84(+0)	3.04(+0)	M1
11 688.429	10 138.18	5/2	18 693.65	1/2		1.53(−4)	6.32(−5)	5.45(−4)	E2
12 214.442	10 859.06	7/2	19 046.09	5/2	3.46(+0)	3.38(+0)	2.56(+0)	2.78(+0)	M1
12 352.008	10 950.24	3/2	19 046.09	5/2	1.12(−1)	1.13(−1)	5.45(−2)	6.43(−2)	M1
12 436.465	4453.76	15/2	12 494.63	11/2		1.96(−3)	6.56(−4)	5.33(−5)	E2
12 914.207	10 950.24	3/2	18 693.65	1/2	7.52(−1)	7.21(−1)	5.38(−1)	6.10(−1)	M1
12 945.034	9370.66	3/2	17 095.63	3/2	1.27(+0)	1.17(+0)	8.80(−1)	1.17(+0)	M1
13 556.271	10 032.92	9/2	17 409.58	11/2	4.24(−2)	2.30(−2)	3.21(−2)	3.38(−1)	M1
13 727.967	11 761.69	9/2	19 046.09	5/2		6.69(−6)	1.68(−5)	1.55(−4)	E2
14 006.034	2893.14	13/2	10 032.92	9/2		3.51(−4)	1.38(−4)	4.49(−6)	E2
14 373.082	10 138.18	5/2	17 095.63	3/2	1.63(+0)	1.49(+0)	1.07(+0)	1.35(+0)	M1
14 856.501	10 032.92	9/2	16 763.98	9/2	4.19(−2)	1.02(−1)	3.10(+0)	1.80(+0)	M1
15 092.517	10 138.18	5/2	16 763.98	9/2		5.03(−4)	2.77(−4)	6.62(−4)	E2
15 265.964	10 859.06	7/2	17 409.58	11/2		1.01(−3)	6.54(−4)	4.98(−3)	E2
16 034.455	10 859.06	7/2	17 095.63	3/2		6.74(−6)	5.35(−7)	3.81(−4)	E2
16 272.360	10 950.24	3/2	17 095.63	3/2	1.96(+0)	2.01(+0)	1.27(+0)	1.54(+0)	M1
16 466.814	9370.66	3/2	15 443.48	7/2		4.81(−4)	3.66(−4)	8.28(−4)	E2
16 511.950	10 032.92	9/2	16 089.14	13/2		7.11(−4)	6.82(−4)	2.44(−4)	E2
16 935.030	10 859.06	7/2	16 763.98	9/2	1.01(+0)	1.10(+0)	1.21(+0)	4.33(−1)	M1

(Continued.)

Table 3. (Continued.)

λ_{vac} (Å)[a]	Lower level[b] E (cm^{-1})	J	Upper level[b] E (cm^{-1})	J	gA (s^{-1}) ($A(B) = A \times 10^B$) Previous[c]	HFR[d]	MCDHF-A[d]	MCDHF-B[d]	Type > 1%
17 629.813	10 032.92	9/2	15 705.13	9/2		1.90(+0)	1.21(−2)	1.14(−4)	M1
17 705.727	11 761.69	9/2	17 409.58	11/2		7.78(−2)	8.62(−2)	1.82(−1)	M1+E2
17 963.158	10 138.18	5/2	15 705.13	9/2		4.28(−4)	2.66(−4)	8.52(−6)	E2
18 482.375	10 032.92	9/2	15 443.48	7/2		5.08(−2)	1.48(−1)	5.52(−1)	M1
18 849.075	10 138.18	5/2	15 443.48	7/2		4.46(−1)	1.23(−1)	1.69(−1)	M1
19 385.518	13 887.60	7/2	19 046.09	5/2		5.77(−2)	4.33(−2)	1.56(−1)	M1
19 427.170	12 494.63	11/2	17 642.06	15/2		3.95(−4)	3.51(−4)	6.43(−6)	E2
19 990.844	11 761.69	9/2	16 763.98	9/2		3.20(+0)	5.61(+0)	1.80(+0)	M1
20 346.087	12 494.63	11/2	17 409.58	11/2		1.81(+0)	1.16(+0)	1.46(+0)	M1
20 581.468	14 187.35	5/2	19 046.09	5/2		2.62(−3)	3.12(−3)	2.42(−2)	M1
20 635.278	10 859.06	7/2	15 705.13	9/2		3.09(−1)	2.36(−1)	4.85(−1)	M1
20 761.145	9370.66	3/2	14 187.35	5/2		1.32(−2)	2.85(−3)	4.93(−4)	M1+E2
21 813.010	10 859.06	7/2	15 443.48	7/2		4.73(−1)	1.99(−1)	1.51(−1)	M1
22 138.882	9370.66	3/2	13 887.60	7/2		5.61(−5)	1.68(−5)	1.23(−5)	E2
22 191.155	14 187.35	5/2	18 693.65	1/2		2.61(−5)	1.02(−5)	6.85(−7)	E2
22 255.655	10 950.24	3/2	15 443.48	7/2		2.19(−6)	5.55(−7)	3.26(−6)	E2
23 108.297	11 761.69	9/2	16 089.14	13/2		3.33(−5)	2.33(−5)	1.89(−6)	E2
23 422.769	12 494.63	11/2	16 763.98	9/2		1.48(+0)	3.64(−1)	8.90(−2)	M1
24 070.691	10 032.92	9/2	14 187.35	5/2		1.60(−7)	3.78(−7)	1.81(−5)	E2
24 696.419	10 138.18	5/2	14 187.35	5/2		6.47(−3)	1.03(−3)	6.24(−4)	M1+E2
25 358.570	11 761.69	9/2	15 705.13	9/2		1.89(+0)	3.88(−1)	1.10(+0)	M1
25 942.491	10 032.92	9/2	13 887.60	7/2		8.98(−1)	7.33(−1)	6.90(−1)	M1
26 670.792	10 138.18	5/2	13 887.60	7/2		9.87(−1)	9.31(−1)	9.03(−1)	M1
27 160.702	11 761.69	9/2	15 443.48	7/2		1.74(−3)	9.49(−5)	2.43(−3)	M1
27 757.653	15 443.48	7/2	19 046.09	5/2		1.42(−3)	3.02(−6)	2.48(−3)	M1
27 820.204	12 494.63	11/2	16 089.14	13/2		2.99(−4)	2.23(−4)	5.10(−4)	M1
28 393.120	13 887.60	7/2	17 409.58	11/2		2.83(−6)	1.62(−6)	3.14(−6)	E2
30 045.459	10 859.06	7/2	14 187.35	5/2		2.47(−2)	1.71(−2)	2.60(−2)	M1
30 891.752	10 950.24	3/2	14 187.35	5/2		1.90(−5)	1.77(−6)	4.21(−7)	M1
31 147.796	12 494.63	11/2	15 705.13	9/2		3.61(−3)	3.68(−1)	6.75(−1)	M1
31 171.778	13 887.60	7/2	17 095.63	3/2		8.59(−7)	1.17(−8)	3.54(−9)	E2
32 728.725	1398.34	11/2	4453.76	15/2		8.14(−9)	5.38(−9)	1.34(−9)	E2
33 019.211	10 859.06	7/2	13 887.60	7/2		5.18(−1)	5.39(−1)	4.85(−1)	M1+E2
33 911.525	12 494.63	11/2	15 443.48	7/2		1.19(−7)	7.04(−10)	2.90(−11)	E2
34 044.176	10 950.24	3/2	13 887.60	7/2		6.40(−8)	1.42(−9)	7.96(−10)	E2
34 384.585	14 187.35	5/2	17 095.63	3/2		6.44(−5)	3.55(−5)	2.27(−4)	M1
34 564.522	0.00	9/2	2893.14	13/2		9.58(−9)	6.61(−9)	4.58(−5)	E2
34 765.921	13 887.60	7/2	16 763.98	9/2		3.69(−3)	3.63(+0)	5.99(−1)	M1
38 810.384	14 187.35	5/2	16 763.98	9/2		2.29(−11)	7.53(−9)	3.62(−12)	E2
40 622.169	10 032.92	9/2	12 494.63	11/2		1.63(+0)	1.76(+0)	1.93(+0)	M1
41 225.893	11 761.69	9/2	14 187.35	5/2		5.05(−8)	4.71(−8)	1.12(−7)	E2
43 819.097	16 763.98	9/2	19 046.09	5/2		9.60(−7)	3.81(−7)	1.06(−5)	E2
47 038.680	11 761.69	9/2	13 887.60	7/2		3.21(−2)	1.86(−2)	1.17(−2)	M1
50 862.113	15 443.48	7/2	17 409.58	11/2		1.57(−8)	2.98(−10)	5.48(−11)	E2
51 269.957	17 095.63	3/2	19 046.09	5/2		2.82(−1)	2.75(−1)	2.05(−1)	M1
55 019.725	13 887.60	7/2	15 705.13	9/2		1.14(+0)	9.99(−3)	4.52(−2)	M1
57 844.595	10 032.92	9/2	11 761.69	9/2		5.95(−1)	5.25(−1)	7.82(−1)	M1
58 669.952	15 705.13	9/2	17 409.58	11/2		1.04(+0)	1.26(+0)	8.16(−1)	M1
60 527.192	15 443.48	7/2	17 095.63	3/2		1.20(−7)	6.21(−8)	1.36(−7)	E2
61 140.764	10 859.06	7/2	12 494.63	11/2		1.68(−7)	6.39(−8)	2.83(−8)	E2
61 594.939	10 138.18	5/2	11 761.69	9/2		6.49(−8)	3.34(−8)	1.65(−8)	E2
62 577.440	17 095.63	3/2	18 693.65	1/2		5.52(−2)	6.85(−2)	4.97(−2)	M1
63 307.968	9370.66	3/2	10 950.24	3/2		9.88(−3)	5.92(−3)	4.83(−3)	M1
64 077.098	2893.14	13/2	4453.76	15/2		2.00(+0)	1.96(+0)	1.91(+0)	M1
64 272.309	13 887.60	7/2	15 443.48	7/2		1.24(−2)	9.05(−3)	1.58(−2)	M1
64 394.818	16 089.14	13/2	17 642.06	15/2		7.07(−1)	7.37(−1)	7.04(−1)	M1
65 885.701	14 187.35	5/2	15 705.13	9/2		8.15(−10)	1.37(−10)	6.70(−10)	E2
66 898.582	1398.34	11/2	2893.14	13/2		2.28(+0)	2.26(+0)	2.26(+0)	M1
67 186.240	9370.66	3/2	10 859.06	7/2		3.42(−8)	2.08(−8)	1.44(−8)	E2

(Continued.)

Table 3. (Continued.)

71 513.366	0.00	9/2	1398.34	11/2	1.37(+0)	1.39(+0)	1.37(+0)	M1
71 789.055	12 494.63	11/2	13 887.60	7/2	1.62(−8)	6.06(−9)	7.78(−10)	E2
75 728.891	15 443.48	7/2	16 763.98	9/2	6.65(−1)	1.24(−1)	3.13(−2)	M1
75 732.332	16 089.14	13/2	17 409.58	11/2	1.37(−6)	5.13(−7)	1.09(−6)	M1
79 609.595	14 187.35	5/2	15 443.48	7/2	5.56(−1)	6.00(−1)	4.72(−1)	M1
94 442.083	15 705.13	9/2	16 763.98	9/2	5.77(−3)	3.38(−3)	3.10(−3)	M1
110 787.366	10 859.06	7/2	11 761.69	9/2	1.60(−1)	1.64(−1)	1.39(−1)	M1
121 044.859	10 032.92	9/2	10 859.06	7/2	1.89(−2)	1.69(−2)	5.03(−2)	M1
123 143.610	10 138.18	5/2	10 950.24	3/2	3.30(−4)	2.40(−4)	2.00(−4)	M1
130 289.764	9370.66	3/2	10 138.18	5/2	1.17(−1)	1.13(−1)	1.39(−1)	M1
136 436.816	11 761.69	9/2	12 494.63	11/2	9.91(−3)	8.06(−3)	2.24(−3)	M1
138 719.343	10 138.18	5/2	10 859.06	7/2	1.32(−1)	1.21(−1)	7.11(−2)	M1
148 183.273	16 089.14	13/2	16 763.98	9/2	9.19(−10)	1.09(−9)	2.82(−8)	E2
154 894.672	16 763.98	9/2	17 409.58	11/2	2.40(−2)	2.43(−2)	2.35(−2)	M1
260 409.885	15 705.13	9/2	16 089.14	13/2	8.08(−11)	2.82(−12)	3.03(−13)	E2
283 736.239	18 693.65	1/2	19 046.09	5/2	9.28(−10)	6.95(−11)	5.99(−11)	E2
382 189.948	15 443.48	7/2	15 705.13	9/2	3.62(−3)	6.96(−3)	2.85(−2)	M1
430 144.529	17 409.58	11/2	17 642.06	15/2	3.59(−12)	2.34(−12)	1.70(−12)	E2

[a] Vacuum wavelengths deduced from the experimental energy levels taken from the NIST database (Kramida *et al* 2024).
[b] Experimental energy level values from Kramida *et al* (2024).
[c] From Li *et al* (2016).
[d] From the present work.

Table 4. Strongest forbidden lines ($gA > 10^{-1}$ s^{-1}) in Pr III.

λ (Å)[a]	gA (s^{-1})[b]	λ (Å)[a]	gA (s^{-1})[b]	λ (Å)[a]	gA (s^{-1})[b]
6367.346	1.76(−1)	9012.021	2.36(+0)	16 935.030	1.10(+0)
6780.157	7.23(+0)	9649.389	9.76(−1)	17 629.813	1.90(+0)
6806.981	6.67(+0)	9967.188	5.71(+0)	18 849.075	4.46(−1)
6888.741	4.38(−1)	10 335.458	2.41(−1)	19 990.844	3.20(+0)
6989.688	7.28(−1)	10 415.050	5.51(+0)	20 346.087	1.81(+0)
7048.533	2.70(−1)	11 225.978	5.48(−1)	20 635.278	3.09(−1)
7119.901	2.22(−1)	11 581.339	3.71(+0)	21 813.010	4.73(−1)
7200.668	1.73(−1)	12 214.442	3.38(+0)	23 422.769	1.48(+0)
7209.369	1.39(−1)	12 352.008	1.13(−1)	25 358.570	1.89(+0)
7578.054	3.86(+0)	12 914.207	7.21(−1)	25 942.491	8.98(−1)
7582.478	1.12(+1)	12 945.034	1.17(+0)	26 670.792	9.87(−1)
7718.539	3.02(−1)	14 373.082	1.49(+0)	33 019.211	5.18(−1)
7805.189	1.48(−1)	14 856.501	1.02(−1)	40 622.169	1.63(+0)
8502.180	9.99(−1)	16 272.360	2.01(+0)	51 269.957	2.82(−1)

[a] Vacuum wavelengths deduced from the experimental energy levels (Kramida *et al* 2024).
[b] Weighted transition probabilities calculated in the present work using the HFR method. A(B) stands for A $\times$ 10^B.

lines (at $\lambda = 19\,990.844, 20\,346.087, 20\,635.278, 21\,813.010, 23\,422.769$ Å) fall within the first range around 2.1 μm while no lines appear in the second range around 4.4 μm. It is however interesting to note that the 5 [Pr III] lines mentioned above imply an upper level of the $4f^3$ configuration having an energy equal to 15 443.48, 15 705.13, 16 763.98 or 17 409.58 cm^{-1}, i.e. located above a couple of $4f^2 5d$ levels of the even parity. These $4f^3$ levels can therefore also be depopulated towards these $4f^2 5d$ levels via allowed E1 transitions. Nevertheless, most of these E1 transitions should appear outside the two features at ∼2.1 μm and ∼4.4 μm if we estimate their wavelengths from the experimentally known energy levels available in the NIST database (Kramida *et al* 2024). The only exceptions are the $4f^3$ – $4f^2 5d$ transitions from 17 409.58 cm^{-1} ($J = 11/2$) to 12 846.66 cm^{-1} ($J = 9/2$), from 15 705.13 cm^{-1} ($J = 9/2$) to 13 352.10 cm^{-1} ($J = 11/2$) and from 16 763.98 cm^{-1} ($J = 9/2$) to 14 558.82 cm^{-1} ($J = 9/2$) for which the Ritz wavelengths are 21 915.791, 42 498.396 and 45 348.183 Å, respectively. These E1 lines could also contribute to the observed features observed in the *JWST* emission spectrum of GRB 23 0307A.

5. Conclusions

Transition probabilities for M1 and E2 lines within the $4f^3$ ground configuration of Pr III were computed in the present work. Different computational strategies based on two independent theoretical methods, i.e. the pseudo-relativistic HFR

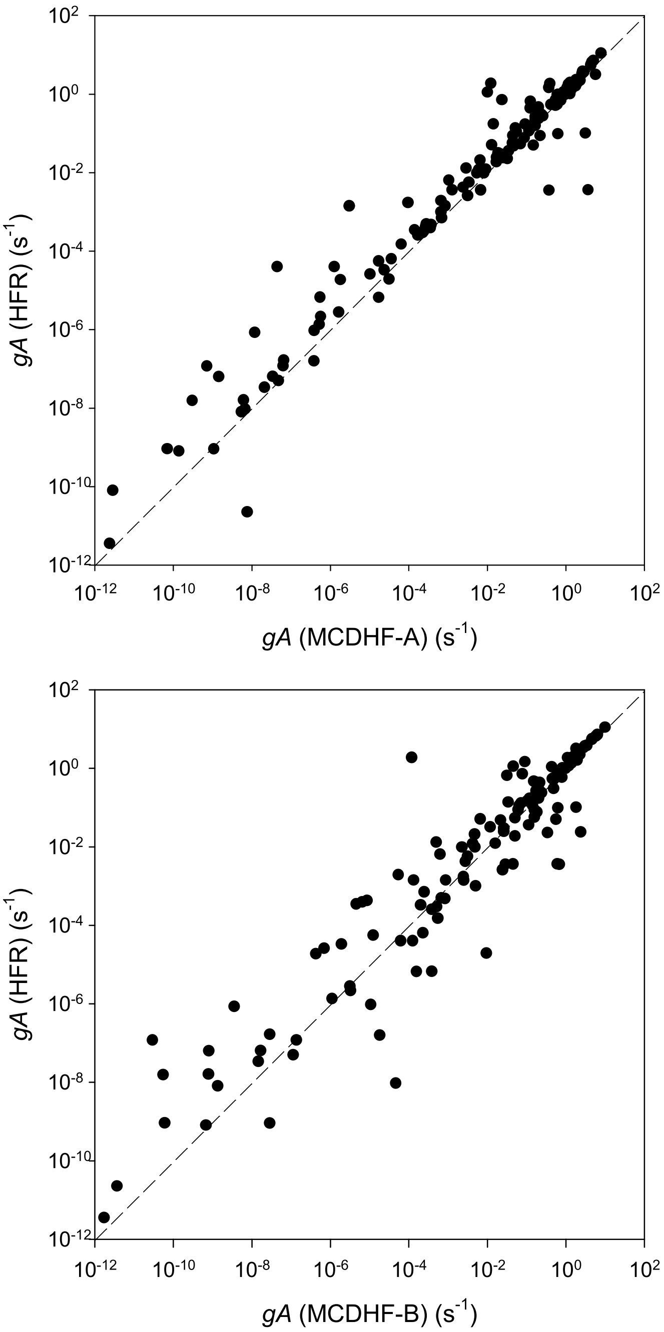

Figure 1. Comparison between transition probabilities computed for forbidden lines in Pr III using HFR and MCDHF methods.

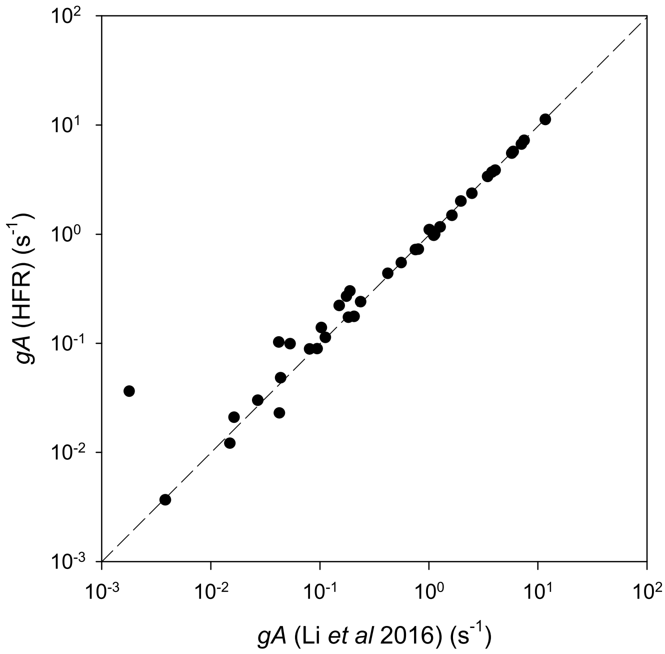

Figure 2. Comparison between transition probabilities computed for forbidden lines in Pr III using HFR and the results published by Li *et al* (2016).

and the fully MCDHF methods, were used in the calculations. This allowed us to provide a new set of radiative decay rates whose accuracy was estimated to be within a factor of two for the most intense forbidden lines thanks to detailed comparisons between the results obtained with the different approaches. From these new atomic parameters, a list of [Pr III] transitions that could be observed on the astrophysical spectra recorded with the *NIRS* instrument onboard the *JWST* was established, among which a few lines could contribute to the particular feature located at $\sim$2.1 μm on the emission spectrum of GRB 23 0307A at T_0+29 d (Gillanders *et al* 2023).

Data availability statement

All data that support the findings of this study are included within the article (and any supplementary files).

Acknowledgments

PP and PQ are, respectively, Research Associate and Research Director of the Belgian Fund for Scientific Research F.R.S. - FNRS. This project has received funding from the FWO and F.R.S. - FNRS under the Excellence of Science (EOS) programme (Numbers 0.0228.18 and 0.0004.22). Part of the atomic calculations were made with computational resources provided by the Consortium des Equipements de Calcul Intensif (CECI), funded by the F.R.S. - FNRS under Grant No. 2.5020.11 and by the Walloon Region of Belgium.

ORCID iDs

L Maison https://orcid.org/0009-0009-7897-7894
P Palmeri https://orcid.org/0000-0002-4372-6798
P Quinet https://orcid.org/0000-0002-3937-2640

References

Abbott B P, Abbott R, Abbott T D, Acernese F and Ackley K 2017 *Phys. Rev. Lett.* **119** 161101

Biémont E, Garnir H P, Palmeri P, Quinet P, Li Z S and Zhang Z G S S 2001 *Phys. Rev.* A **64** 022503

Cowan R D 1981 *The Theory of Atomic Structure and Spectra* (California University Press)

Froese Fischer C, Gaigalas G, Jönsson P and Biéron J 2019 *Comput. Phys. Commun.* **237** 184

Gillanders J H, McCann M, Sim A S, Smartt S J and Ballance C P 2021 *Mon. Not. R. Astron. Soc.* **506** 3560
Gillanders J H, Troja E, Fryer C L, Ristic M and O'Connor B 2023 arXiv:2308.00633
Grant I P 2007 *Relativistic Quantum Theory of Atoms and Molecules* (*Theory and Computations*) (Springer)
Jakobsen P, Ferruit P, Alves de Oliveira C, Arribas S and Bagnasco G 2022 *Astron. Astrophys.* **661** A80
Kasen D, Metzger B, Barnes J, Quataert E and Ramirez-Ruiz E 2017 *Nature* **551** 80
Kasliwal M M, Kase D, Lau R M, Perley D A and Rosswog S 2022 *Mon. Not. R. Astron. Soc.* **510** L7
Kramida A, Ralchenko Y and Reader J 2024 NIST atomic spectra database (available at: https://physics.nist.gov/asd)
Li H, Kuang X Y and Yeung Y Y 2016 *J. Lumin.* **170** 380
Li Y, Gaigalas G, Li W, Chen C and Jönsson P 2023 *Atoms* **11** 70
Maison L, Palmeri P Quinet P 2024 *J. Phys. B: At. Mol. Opt. Phys.* **57** 105002
Martin W C, Zalubas R and Hagan L 1978 *Nat. Stand. Ref. Data Ser. NSRDS-NBS* 60
Palmeri P, Quinet P, Frémat Y and Wyart J F B E 2000 *Astrophys. J. Suppl.* **129** 367
Pian E 2023 *Universe* **9** 105
Pian E, D'Avanzo P, Benetti S, Branches M and Brocato E 2017 *Nature* **551** 67
Siegel D M 2022 *Nat. Rev. Phys.* **4** 306
Smartt S J, Chen T W, Jerkstrand A, Coughlin M and Kankare E 2017 *Nature* **551** 75